

Spin structure of the deuteron by using $d(\vec{e}, e'\vec{p})$

W. Bertozzi, Z. Chai, O. Gayou (co-spokesperson), S. Gilad¹ (co-spokesperson),
B. Ma, P. Monaghan, Y. Qiang, L. Wan, Y. Xiao, C. Zhang
Laboratory for Nuclear Science, Massachusetts Institute of Technology, Cambridge, MA

Z.-L. Zhou (co-spokesperson)
Schlumberger-Doll Research, Ridgefield, CT

S. Širca (co-spokesperson)
Dept. of Physics, University of Ljubljana, Slovenia

D. W. Higinbotham, B. Reitz
Thomas Jefferson National Accelerator Facility, Newport News, VA

P. E. Ulmer, L. Weinstein
Old Dominion University, Norfolk, VA

J. J. Kelly
Dept. of Physics, University of Maryland, College Park, MD

S. Jeschonnek
Dept. of Physics, Ohio State University, Columbus, OH

M. Epstein, D. Margaziotis
California State University, Los Angeles, CA

A. J. Sarty
Dept. of Astronomy and Physics, St. Mary's University, Halifax, Nova Scotia, Canada

B. Norum, K. Wang
Dept. of Physics, University of Virginia, Charlottesville, VA

W. U. Boeglin, P. Markowitz, J. Reinhold
Dept. of Physics, Florida International University, Miami, FL

and

Hall A Collaboration

¹Contact person; e-mail: sgilad@mitlns.mit.edu

Abstract

We propose a measurement of double-polarization observables in the $d(\vec{e}, e'\vec{p})$ reaction to investigate the spin structure of the deuteron. The individual components P'_x and P'_z , measured in parallel kinematics and in a broad range of p_m , will reveal the dynamics of the deuteron spin structure and the manifestation of the D -state component in the deuteron ground-state wave-function. This will show to what extent the deuteron can be used as a neutron target. In contrast, the P_y^0 and the P'_x/P'_z ratio will mirror the underlying spin-dependent reaction mechanism.

When using the P'_x/P'_z ratio to extract information on the electric form-factors, modern models surprisingly suggest that the D -state has little effect even at high missing momenta, while the effects from the spin-dependent reaction mechanism are enormous. A detailed study of these is extremely important to learn when the deuteron can be used as an effective neutron target, and also for the few-body physics.

We will measure the cross-sections and the recoil polarization components P'_x , P'_z , and P_y^0 as functions of p_m . Consequently, we will be able to extract the individual structure functions f_L , f_T , f_{LT}^n , f_{LT}^t , and f_T^1 in the corresponding region of p_m . The experiment requires a $70\text{ }\mu\text{A}$ polarized beam at 0.845 GeV and 3.2 GeV, and the standard HRS configuration of Hall A with FPP capability. We request 243 hours of beam time.

Contents

1	Introduction and physics motivation	4
1.1	Existing double-polarization experiments	5
1.2	Relation to other JLab experiments	7
2	Polarized deuteron electro-disintegration	7
3	Choice of kinematics	9
3.1	Model calculations	11
3.2	The physical meaning of polarization components	13
3.3	Parallel vs. perpendicular kinematics	15
3.4	Separated structure functions	16
4	Experimental equipment and methods	18
4.1	Focal-Plane Polarimeter	18
4.2	FPP systematical uncertainties	21
5	Counting rates and beam-time request	21
5.1	Systematical uncertainties	23
6	Conclusions	24
	References	24

1 Introduction and physics motivation

One of the principal goals of nuclear physics is the understanding of nuclear structure and of the underlying nucleon-nucleon (NN) interaction. The deuteron certainly represents one of the most attractive candidates for such an investigation. The experimental study of the large-momentum behaviour of the deuteron wave-function has been of particular importance and has been used for a determination of the short-range properties of nuclear forces. The deuteron has also been used successfully as a neutron target, giving access to the neutron form-factors. In this case, to extract precise information on either form-factor, not only a detailed understanding of the deuteron structure is required but also a quantitative understanding of the reaction mechanism, such as the effects of relativity, two-body currents (MEC and IC) and final-state interaction (FSI). These interaction effects can be most clearly studied in the two-nucleon system as it is relatively easily calculable.

The continued interest in polarized electro-disintegration of the deuteron reflects the fact that it provides a very powerful tool to investigate the structure of the two-nucleon system and its electromagnetic properties [1, 2, 3]. Presently, several state-of-the-art calculations for the deuteron electro-disintegration are available in both non-relativistic and relativistic frameworks (see for example [4, 5, 6, 7, 8]). On the experimental side, many measurements have been performed especially in the past decade. However, with the exceptions listed below, data from deuteron electro-disintegration are still limited mostly to spin-independent observables (cross-sections and unpolarized structure functions).

Only recently, with the advances in new techniques like recoil polarimetry and polarized targets, measurements involving polarization degrees-of-freedom became feasible. Double-polarization observables are an excellent means to increase the sensitivity to the dynamical features of the deuteron. The proposed experiment has been designed to employ spin observables in the $d(\vec{e}, e'\vec{p})$ reaction for an enhanced investigation of the deuteron's dynamical spin structure. Very few measurements exist to-date, especially in regions where the D -state component of the ground-state wave-function is expected to play a key role. The results will also provide much better information on the extent to which the deuteron can be used as a neutron target in order to extract neutron form-factors, and on the spin structure of the deuteron.

From the theoretical standpoint, the simultaneous measurements of cross-sections and several double-polarization observables will yield stringent constraints on theoretical models with both non-relativistic and relativistic approaches. In addition, they will give insight into the reaction mechanism, in particular into the spin-dependent part of the FSI. This is expected to be helpful in answering the questions to what extent the traditional impulse approximation is still valid, whether a vigorous coupled-channel approach is needed, or whether Glauber calculations of FSI [8] are applicable at these energies.

By using the double-polarization technique, we will be able not only to suppress the cross-section related systematical uncertainties, but also to enhance sensitivities to small quantities which can not be resolved by cross-section measurements alone. In particular, the double-polarization method will allow us to directly access five individual electro-disintegration structure functions. With the instrumental capabilities of Hall A and CEBAF, we shall be able to cover a broad enough kinematical range to access all recoil polarization components and their ratios with sufficient accuracy. We expect that these experimental information will promote considerably our present understanding of the dynamics of the deuteron.

1.1 Existing double-polarization experiments

At NIKHEF, the spin-momentum correlation parameter $A_{ed}^V(\theta_d = 90^\circ, \phi_d = 0^\circ)$ has been measured for the quasi-elastic $\vec{d}(\vec{e}, e'p)$ process at $Q^2 = 0.21 \text{ (GeV/c)}^2$ and for $p_m \lesssim 400 \text{ MeV/c}$ [9]. The cross-section for this process can be expressed in terms of the vector (P_1^d) and tensor (P_2^d) polarizations of the target and vector ($A_{d/ed}^V$) and tensor ($A_{d/ed}^T$) analyzing powers and spin-correlation parameters which depend on the orientation of the target spin,

$$\sigma = \sigma_0 \left[1 + P_1^d A_d^V + P_2^d A_d^T + h \left(P_1^d A_{ed}^V + P_2^d A_{ed}^T \right) \right].$$

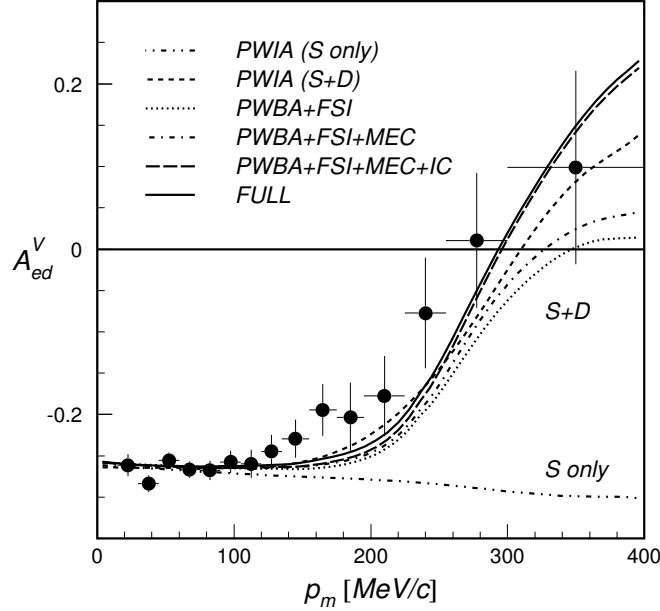


Fig. 1 — The spin correlation parameter $A_{ed}^V(90^\circ, 0^\circ)$ as a function of missing momentum for the $\vec{d}(\vec{e}, e'p)$ reaction at $Q^2 = 0.21 \text{ (GeV/c)}^2$ [9]. Note that the “S-only” curve differs from a constant only due to the extended acceptance of the detectors.

The correlation parameter $A_{ed}^V(90^\circ, 0^\circ)$ was extracted by measuring the asymmetries in flipping the deuteron vector polarization in the scattering plane and perpendicular to \mathbf{q} while keeping the tensor polarization fixed. In naive PWIA, the asymmetry A_{ed}^V depends on the kinematics, the electro-magnetic form-factors of the proton, and on the vector polarization P_1^d of the deuteron. The latter is related to the polarization of the proton P_z^p inside the deuteron by

$$P_z^p = \sqrt{\frac{2}{3}} P_1^d \left(P_S - \frac{1}{2} P_D \right),$$

where P_S and P_D represent the S - and D -state probability densities of the deuteron ground-state wave-function [10]. In this approximation, $A_{ed}^V(90^\circ, 0^\circ)$ is equal to the elastic asymmetry for scattering off a free proton.

With the inclusion of neutron contributions (PWBA) and by accounting for spin-dependent effects of final-state interactions (FSI), meson-exchange currents (MEC), isobar configurations (IC), and relativistic corrections (RC), a measurement of A_{ed}^V yields a much more detailed account of the mechanism through which spin and momentum become correlated (see Fig. 1).

The low- p_m region has been used as a calibration in the extraction of the neutron form-factors. In contrast, the characteristic momentum dependence of the measured $A_{\text{ed}}^V(90^\circ, 0^\circ)$ at high p_m clearly demonstrated an increasing effect of the D -state in the deuteron ground-state wave-function and of the reaction dynamics. The question is whether these effects can be studied with another experimental technique.

It has been shown [10] that by measuring the ejected proton polarization components instead of measuring beam-target asymmetries, equivalent information can be obtained. In naive PWIA language, the recoil polarization components are related to the elastic asymmetries for scattering off a free proton, $P'_x \sim A_{\text{ep}}^x$ and $P'_z \sim -A_{\text{ep}}^z$. With the same detailed knowledge on the deuteron structure, we intend to exploit this correspondence to investigate the mechanisms by which spins and momenta of the nucleons within the deuteron are interconnected. The spin transfer to the proton depends on the missing momentum, and in turn depends on the relative orbital angular momentum (and the corresponding ground-state wave-function component) in the deuteron.

Several measurements of deuteron electro-disintegration utilizing the Focal-Plane Polarimetry (FPP) method have been done in the past [11, 12, 13, 14]. However, the existing data are very sparse, and the experiments either tried to access the deuteron spin structure through angular distributions (which have strong dependencies and are very sensitive to the reaction mechanism, see below), or through Q^2 -dependencies. When Q^2 -dependencies are studied, one usually tries to choose a kinematical range in which nuclear effects are believed to be small and hence the deuteron can be used as a free proton (or neutron) target. This allows one to extract the electro-magnetic form-factors of the nucleon since the two helicity-dependent recoil polarization components P'_x and P'_z contain the terms $G_E^p G_M^p$, respectively:

$$P'_x = -2 \frac{h}{I_0} \sqrt{\tau(1+\tau)} G_E^p G_M^p \tan \frac{\theta_e}{2}, \quad (1)$$

$$P'_z = \frac{h(E_e + E'_e)}{I_0 M_p} \sqrt{\tau(1+\tau)} (G_M^p)^2 \tan^2 \frac{\theta_e}{2}. \quad (2)$$

Here h is the electron helicity, $I_0 = (G_E^p)^2 + (\tau/\varepsilon)(G_M^p)^2$ is the unpolarized cross-section (excluding σ_{Mott}), and $\tau \equiv Q^2/4M_p^2$. The value of G_M^p at $Q^2 = 0$ is normalized to $\mu_p/\mu_B = 2.79$. By taking the ratio of the polarization components one obtains

$$\frac{G_E^p}{G_M^p} = -\frac{P'_x}{P'_z} \frac{E_e + E'_e}{2M_p} \tan \frac{\theta_e}{2}. \quad (3)$$

In addition, one usually takes the ratio of ratios, $(P'_x/P'_z)_d / (P'_x/P'_z)_p$ to cancel out some systematical uncertainties. The “super-ratios” turn out to be around 1 to within 5% regardless of the kinematics, in accordance with the expectations (with a somewhat higher value of 1.2 of the $p_m = 160 \text{ MeV}/c$ point in perpendicular kinematics of [14]). Available data at $p_m = 0$ are shown in Fig. 2.

We therefore intend to strictly maintain parallel kinematics by increasing p_m and letting ω float along with Q^2 fixed (see Fig. 4 and the discussion on the choice of kinematics in Section 3). The parallel p_m -dependence of the double-polarization observables should then yield a picture of the deuteron spin structure complementary to the NIKHEF measurements with the polarized target. The NIKHEF result [9] shows that the region with $200 \lesssim p_m \lesssim 350 \text{ MeV}/c$ where the data on the spin-momentum correlation parameter $A_{\text{ed}}^V(90^\circ, 0^\circ)$ deviate from calculations needs to be explored in more detail. Further reasons for parallel kinematics are given in Section 3.

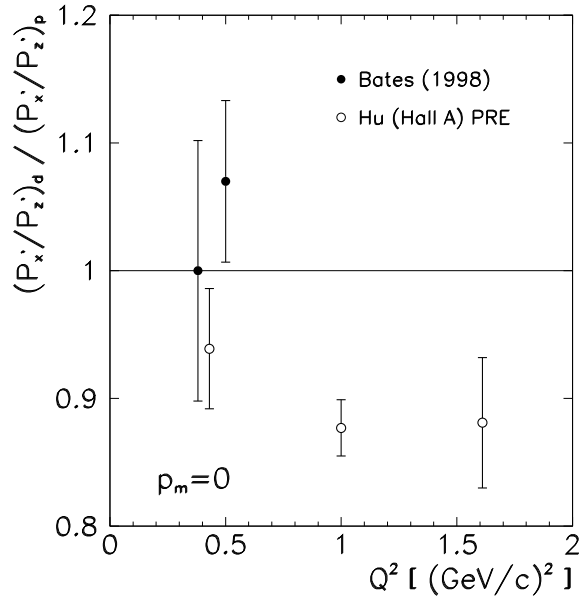


Fig. 2 — The Q^2 -dependence of the ratios of polarization transfer coefficients for deuteron and proton $(P'_x/P'_z)_d / (P'_x/P'_z)_p$ extracted from the $d(\vec{e}, e' \vec{p})$ reaction at $p_m = 0$ [11, 14].

1.2 Relation to other JLab experiments

There was only one double-polarization experiment in Hall A. Polarization transfer coefficients in the $d(\vec{e}, e' \vec{p})$ reaction were measured at $Q^2 = 0.43, 1.00$, and 1.61 (GeV/c) 2 with $p_m = 0$ (parallel kinematics) and for $Q^2 = 1.00$ (GeV/c) 2 with $p_m = 160$ MeV/c (perpendicular kinematics) [14]. The ratios $(P'_x/P'_z)_d / (P'_x/P'_z)_p$ have been extracted. The ratios were determined with much smaller statistical uncertainties than in the measurements at Bates [11]. Only a very weak Q^2 -dependence has been observed for $p_m = 0$ settings, and the ratio is ~ 0.9 for the whole Q^2 -range (see Fig. 2).

2 Polarized deuteron electro-disintegration

A schematic representation of the $d(\vec{e}, e' \vec{p})$ reaction is presented in Fig. 3. The cross section can be written as a sum of terms which include 18 independent structure functions $f_{\alpha\beta}$ in the following form [1, 2, 3]

$$\begin{aligned}
 \frac{d\sigma (1 + \vec{P})}{d\Omega_{e'}^{\text{lab}} dE'^{\text{lab}} d\Omega_{pq}^{\text{cm}}} &= c \left[\left(\rho_L f_L + \rho_T f_T + \rho_{LT} f_{LT} \cos \phi_{pq}^{\text{cm}} + \rho_{TT} f_{TT} \cos 2\phi_{pq}^{\text{cm}} \right) \right. \\
 &+ h \rho'_{LT} f'_{LT} \sin \phi_{pq}^{\text{cm}} \\
 &+ \left(\rho_L f_L^n + \rho_T f_T^n + \rho_{LT} f_{LT}^n \cos \phi_{pq}^{\text{cm}} + \rho_{TT} f_{TT}^n \cos 2\phi_{pq}^{\text{cm}} \right) \\
 &+ \left(\rho_{LT} f_{LT}^l \sin \phi_{pq}^{\text{cm}} + \rho_{TT} f_{TT}^l \sin 2\phi_{pq}^{\text{cm}} \right) \\
 &+ \left. \left(\rho_{LT} f_{LT}^t \sin \phi_{pq}^{\text{cm}} + \rho_{TT} f_{TT}^t \sin 2\phi_{pq}^{\text{cm}} \right) \right]
 \end{aligned}$$

$$\begin{aligned}
& + h \rho'_{LT} f'^n_{LT} \sin \phi_{pq}^{\text{cm}} \\
& + h \left(-\rho'_T f'^1_T - \rho'_{LT} f'^1_{LT} \cos \phi_{pq}^{\text{cm}} \right) + h \left(-\rho'_T f'^t_T - \rho'_{LT} f'^t_{LT} \cos \phi_{pq}^{\text{cm}} \right) \Big] ,
\end{aligned}$$

where c is proportional to the Mott cross section, $\rho_{\alpha\beta}$ are kinematic terms which depend only on the electron kinematics (momentum transfer \mathbf{q} and energy transfer ω). The individual terms can be grouped as

$$\frac{d\sigma}{d\Omega_e^{\text{lab}} dE'^{\text{lab}} d\Omega_{pq}^{\text{cm}}} (1 + \vec{P}) = \sigma_{\phi_{pq}^{\text{cm}}}^0 \left(1 + hA'_{LT} + P_y^0 + P_z^0 + P_x^0 + hP'_y + hP'_z + hP'_x \right) = \sigma_{\phi_{pq}^{\text{cm}}}^h (1 + \vec{P}) ,$$

where A'_{LT} represents the beam-helicity asymmetry while the P^0 s (P' s) are the helicity-independent (dependent) polarization components of the recoiling proton. The “cm” label refers to the center-of-mass frame of the final n-p system.

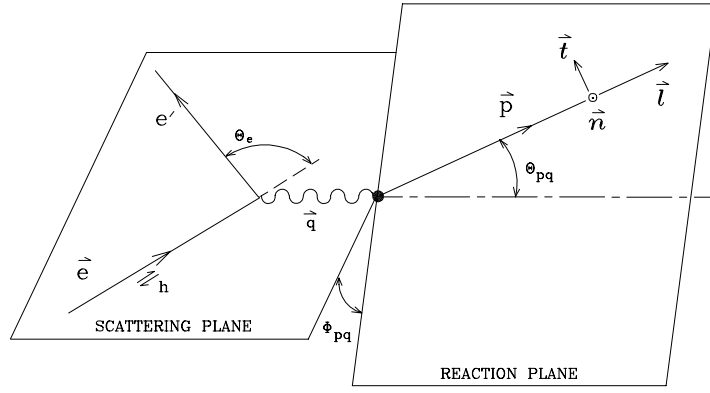


Fig. 3 — Geometry of exclusive electron scattering with polarized electrons and polarized recoil protons. The components of the polarization of the recoil protons are denoted by “t” (transverse to \mathbf{p}), “l” (collinear with \mathbf{p}), and “n” (collinear with $\mathbf{q} \times \mathbf{p}$ and perpendicular to the reaction plane). In the following, we use the correspondence $t \equiv x$, $l \equiv z$, and $n \equiv y$.

For coplanar (in-plane) kinematics the polarization-independent part of the cross-section and the recoil polarization components reduce to

$$\begin{aligned}
\sigma_{\phi_{pq}^{\text{cm}}}^0 &= c \left(\rho_L f_L + \rho_T f_T + \rho_{LT} f_{LT} \cos \phi_{pq}^{\text{cm}} + \rho_{TT} f_{TT} \cos 2\phi_{pq}^{\text{cm}} \right) , \\
P_y^0 &= \frac{c}{\sigma_{\phi_{pq}^{\text{cm}}}^0} \left(\rho_L f_L^n + \rho_T f_T^n + \rho_{LT} f_{LT}^n \cos \phi_{pq}^{\text{cm}} + \rho_{TT} f_{TT}^n \cos 2\phi_{pq}^{\text{cm}} \right) , \\
P_z' &= \frac{c}{\sigma_{\phi_{pq}^{\text{cm}}}^0} \left(-\rho'_T f'^1_T - \rho'_{LT} f'^1_{LT} \cos \phi_{pq}^{\text{cm}} \right) , \\
P_x' &= \frac{c}{\sigma_{\phi_{pq}^{\text{cm}}}^0} \left(-\rho'_T f'^t_T - \rho'_{LT} f'^t_{LT} \cos \phi_{pq}^{\text{cm}} \right) .
\end{aligned}$$

In parallel kinematics, more terms drop out due to conservation laws and implicit θ_{pq}^{cm} -dependencies embedded in the structure functions. The cross-section and the recoil polarization components simplify to

$$\sigma^0 = c \left(\rho_L f_L + \rho_T f_T \right), \quad (4)$$

$$P_y^0 = \frac{c}{\sigma^0} \rho_{LT} f_{LT}^n, \quad (5)$$

$$P_z' = -\frac{c}{\sigma^0} \rho_T' f_T'^1, \quad (6)$$

$$P_x' = -\frac{c}{\sigma^0} \rho_{LT}' f_{LT}'^t. \quad (7)$$

The advantage of measuring polarized structure functions becomes clear when they are expressed in terms of components of the electro-magnetic nuclear current. The polarized structure functions involve products of current components, and smaller components become amplified by larger components by interference. Therefore, a measurement of polarization components in parallel kinematics gives directly the individual spin-dependent structure functions of the deuteron. For example, $f_{LT}'^t$ is proportional to $G_E^p G_M^p \rho_p'(p)$, where $\rho_p'(p)$ is the spin-dependent proton distribution inside the deuteron. In naive PWIA, at small p_m , P_x' would reduce to Eq. (1). It is evident that measuring the polarization components at selected kinematics can isolate small and unknown components and puts a more severe constraint on the theoretical understanding of the spin-dependent deuteron structure.

The simplification to parallel kinematics, when two beam energies are used, allows us to disentangle f_L and f_T in Eq. (4) by means of the Rosenbluth method. The Rosenbluth separations of the response functions have been performed in several labs [15, 16, 17, 19]. However, the data were limited to the region of small missing momenta, and exhibit controversies which perhaps arise through large systematical uncertainties of the extraction from the measured cross-sections. Using the precision spectrometer system and the high quality beam in Hall A, we can separate precisely the longitudinal response from the transverse in the high- p_m region and resolve the existing issue in this respect. In addition, with a different beam energy, but with the ω , q , and p_p in parallel kinematics unaltered, the individual structure functions do not change. However, individual polarization components do change since the kinematical factors (c , ρ s, and the unpolarized cross-section σ_0) change (see Eqs. (5-7)). This additional measurement will provide a cross-check or calibration to our double-polarization measurements using the FPP.

3 Choice of kinematics

The choice of kinematics is based on the achievable kinematical parameters of the JLab/Hall A apparatus versus the only possible alternative at Mainz/A1. The beam energy of 855 MeV at Mainz with the present spectrometer configuration are insufficient to reach the highest proposed p_m of about 350 MeV/c. For example, even at $Q^2 = 0.1 \text{ (GeV/c)}^2$, the maximal proton spectrometer momentum limits the highest achievable p_m to about 300 MeV/c. The achievable range in p_m shrinks even further at higher Q^2 . The figure of merit of the A1 FPP, which can only be installed in the spectrometer with a maximum momentum of 735 MeV/c, will be further reduced by the rapid decrease in the $d(e, e'p)$ cross-sections at high p_m .

The choice of kinematics for Hall A involves several factors. At smaller scattering angles which could be reached by using the septum magnets, the ability to make vertex cuts diminishes. In addition, the transferred polarization components tend to decrease with decreasing scattering

angles. This limits the scattering angles into the $\gtrsim 13^\circ$ region. Possible kinematics with smaller beam energies of 1600 and 2400 MeV yield unsatisfactory FPP efficiencies and figures of merit. This leads to a higher accidentals contamination of the data in the high- p_m region. Regarding momentum transfer, we estimate the value of $Q^2 = 0.5 \text{ (GeV/c)}^2$ to be the highest allowable before $G_E^p(Q^2)$ starts to drop significantly below unity and where e-p effects in the proton knock-out could become too prominent.

$$E_{\text{beam}} = 3200 \text{ MeV}$$

The first kinematics of our choice for JLab/Hall A is therefore at a beam energy of 3200 MeV and $Q^2 = 0.5 \text{ (GeV/c)}^2$, with parallel kinematics for the ejected proton. This gives us a large lever arm on p_m up to 350 MeV/c, with sufficient FPP figures of merit (see below for anticipated FPP performance). The relation between kinematical quantities is shown in Fig. 4, while the proposed kinematics points are listed in Table 1. From the theoretical point of view, pushing Q^2 to this value will help distinguish whether it is sufficient to stay with the impulse approximation in the calculations or resort to coupled-channel calculations or even Glauber theory.

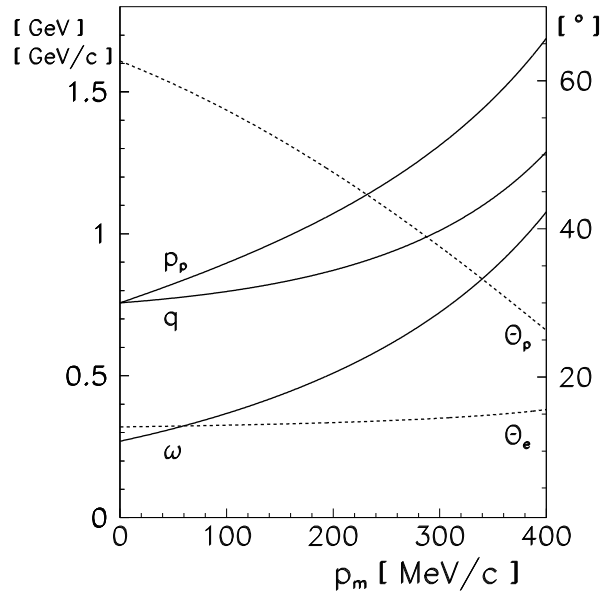


Fig. 4 — Kinematic variables for the beam energy of 3200 MeV as a function of the missing momentum. In parallel kinematics with $\theta_{pq} = 0$, increasing p_m translates into an increase in ω . The electron scattering angle θ_e changes slightly in order to maintain a constant Q^2 .

$$E_{\text{beam}} = 845 \text{ MeV}$$

The second set of kinematics requires a beam energy of 845 MeV to perform the f_L/f_T cross-section separation at $p_m = 100, 150, \text{ and } 200 \text{ MeV/c}$, including a full double-polarization measurement at $p_m = 100 \text{ MeV/c}$. Separating the longitudinal and transverse responses at three different p_m will serve as a useful comparison to existing unpolarized Rosenbluth data. They will provide an important input to the present theoretical and experimental problems that exist in the L/T separation in the low- p_m region [17, 18, 19].

The proposed Rosenbluth separation at $Q^2 = 0.5 \text{ (GeV/c)}^2$ has several advantages over the existing Rosenbluth measurements in which typically $Q^2 \lesssim 0.1 \text{ (GeV/c)}^2$. At low Q , the phase-space is very sensitive to the accuracy in the kinematics, which may cause large systematical errors, and Coulomb distortions can have significant effects on the f_L . At higher Q^2 , these effects will be much smaller. Moreover, as shown in Fig. 11, the reaction mechanism effects are small in the low- p_m (almost no model dependence at $p_m \lesssim 100 \text{ MeV/c}$), which is another beneficial consequence of the relatively high Q^2 . The region around $p_m = 200 \text{ MeV/c}$ is suitable for studies of the model dependence. In addition, with the proton momentum and FPP parameters not being changed, the added polarization measurement at $p_m = 100 \text{ MeV/c}$ will serve as a cross-check to the equivalent measurement with the beam energy of 3200 MeV.

Including the second kinematics set, requiring only a modest addition of beam-time (approximately 1 day, see below), we finally expect to acquire data on f_L and f_T up to $p_m = 200 \text{ MeV/c}$ from the Rosenbluth part, as well as f_T^l , f_{LT}^t , and f_{LT}^n up to $p_m = 350 \text{ MeV/c}$ from the measurement at the higher beam energy.

Table 1 — Proposed kinematics for the beam energies of 845 and 3200 MeV. Note that $Q^2 = -\omega^2/c^2 + |\mathbf{q}|^2 = 0.5 \text{ (GeV/c)}^2$ is constant for all kinematics. The ε denotes the virtual photon polarization.

$E_e \text{ [MeV]}$	p_m	ε	$E'_e \text{ [MeV]}$	$\theta_e \text{ [}^\circ\text{]}$	$p_p \text{ [MeV/c]}$	$\theta_p \text{ [}^\circ\text{]}$	$\omega \text{ [MeV]}$	$ \mathbf{q} \text{ [MeV/c]}$
845	100	0.47	477.3	67.7	897	33.6	367.1	796.7
845	150	0.39	412.7	73.6	978	28.5	431.1	828.2
845	200	0.29	335.8	83.2	1072	22.5	509.2	871.4
3200	100	0.97	2832.3	13.5	897	56.0	367.1	796.7
3200	150	0.96	2767.7	13.6	978	52.0	431.1	828.2
3200	200	0.96	2690.8	13.8	1072	47.6	509.2	871.4
3200	250		2595.6	14.1	1180	42.8	604.3	930.2
3200	300		2476.8	14.4	1312	37.6	723.2	1011.4
3200	350		2322.4	14.9	1476	32.0	875.5	1125.4

3.1 Model calculations

Unpolarized cross-section data, especially in the region of high p_m have yielded very important results [20, 21, 22, 23], and generated much theoretical interest. The calculations for our kinematics have been performed by Prof. Arenhövel and his group [24]. Figure 5 shows the most important Feynman diagrams included in the calculations. The Born approximation neglects the final-state interaction between the outgoing proton-neutron pair and MEC and IC effects, but retains the electro-magnetic interaction with the neutron (diagram b).

The calculations have been done in a semi-relativistic approach in which the leading-order relativistic contributions in the p/M -expansion are included. The two-nucleon bound and scattering states are computed by solving the Schrödinger equation using a realistic NN-potential. The model includes meson-exchange currents consistent with the NN-potential and nucleon resonance configurations. Moreover, contributions from π -, ρ - and ω -exchange currents are also taken into account.

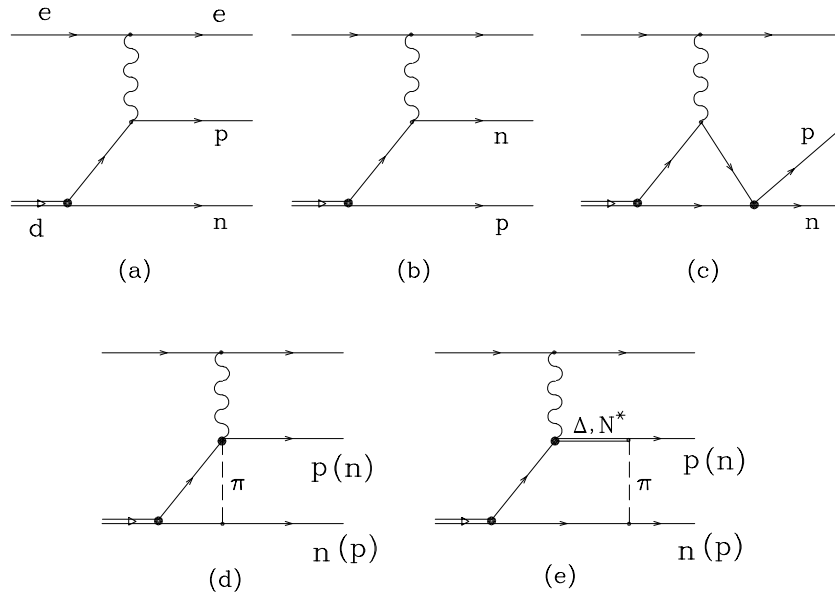


Fig. 5 — Leading Feynman diagrams contributing to the $d(e, e'p)$ process: PWIA e-p scattering (a), PWIA e-n scattering (b), final-state interactions (c), pion-exchange one-body, pair, contact and meson currents (d), and isobar excitations (e).

All model results except coupled-channels (CC) are done with the Bonn r -space potential [25]. The “TOTAL (IA)” label stands for “PWBA+FSI+MEC+IC+REL” in the impulse approximation. The CC method also uses the Bonn potential, but the calculation is done in momentum space. The calculated differential cross-sections are shown in Fig. 6.

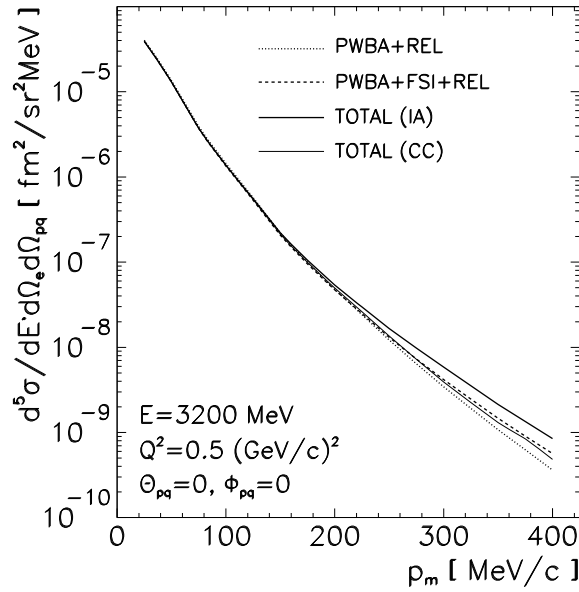


Fig. 6 — The p_m -dependence of the coincidence cross-section in parallel kinematics ($\theta = 0^\circ$) at $E = 3200$ MeV and $Q^2 = 0.5$ (GeV/c) 2 . Here and in the following figures the “TOTAL (IA)” label stands for “PWBA+FSI+MEC+IC+REL” in the impulse approximation.

3.2 The physical meaning of polarization components

The polarization components and the expected data are shown in Figs. 7 and 8. In the following, we discuss the physics content of individual components based on their p_m -behaviour.

P'_z

In the plane-wave picture, and assuming factorization, the RHS of Eqs. (1-2) acquire an additional weight which describes the spin-dependent momentum distribution $\rho'_p(p)$ of the proton within the deuteron. The effects of form-factors and the properties of the wave-function on the polarization components are then cleanly separated. Hence, the dependence of polarization components on p_m will reflect the effects of the D -state at high p_m . When the neutron channel is taken into consideration (diagram (b) in Fig. 5), the amplitude for the process becomes a function of a (G_E^p, G_M^p) part modulated by $\rho'_p(p)$, and a (G_E^n, G_M^n) part modulated by $\rho'_n(p)$, with different weights appearing in the nominators and denominators. Since G_E^n and $\rho'_n(p)$ are small in our kinematics, the neutron channel does not distort significantly the plane-wave picture, and P'_z still carries information on the D -state spin structure at high p_m . This can be seen in Fig. 7 from the difference of PWBA (S+D) and the naive PWIA (S only).

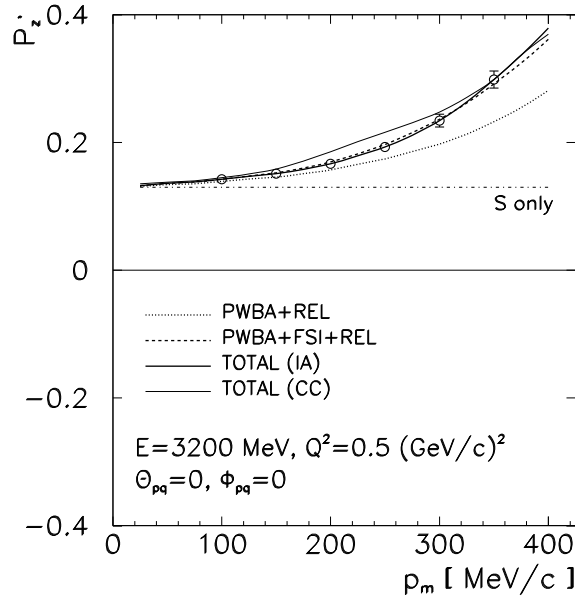


Fig. 7 — The p_m -dependence of P'_z for parallel kinematics ($\theta = 0^\circ$) at $E = 3200 \text{ MeV}$ and $Q^2 = 0.5 (\text{GeV}/c)^2$, with anticipated statistical uncertainties. The “S only” label corresponds to naive PWIA without the D -state.

This remains valid even when one includes MEC and IC. In parallel kinematics, missing momenta of $200 \text{ MeV}/c \lesssim p_m \lesssim 300 \text{ MeV}/c$ roughly map to values of ω corresponding to Δ -excitation, and MEC+IC contribute as much as 50% to the cross-section. A further complication arises from the fact that the pions taking part in the MEC and Δ s in the IC are off-shell. However, behaviour of the magnetic transition form-factors G_M^* for both Δ^0 and Δ^+ excitation are known to be very similar to that of G_M^p . Therefore, the plane-wave picture is still reasonably justified with P'_z . The remaining and physically most interesting effect with increasing p_m originates in relativistic corrections, in-line with the expectation that the proton spin direction becomes modified when the D -state wave-function component starts to take over. Of course, a part of the residual p_m -dependence reflects the underlying spin-dependent FSI which

is present in all polarization components, not only P'_z . The key issue is the p_m -dependence of the spin transfer; we assume the reaction mechanism on top of it to be well controlled.

At small p_m , the P'_z component is almost constant and does not exhibit any model dependence. This is the region which allows for the access to nucleon magnetic form factor as here $P'_z \sim (G_M^p)^2$ (see Eq. (2)).

P'_x and P_y^0

The P'_x component at small p_m is also almost constant and does not exhibit any model dependence. This is the region which allows for the access to the nucleon electric form-factor, as in the plane-wave view, $P'_x \sim G_E^p G_M^p$ according to Eq. (1). With increasing p_m , the effects of the D -state become obvious, which can be seen from the difference of PWBA (S+D) and naive PWIA (S only), similar to the behaviour observed in P'_z .

However, the effects of reaction dynamics are quite different for P'_x . Beyond the plane-wave view, the neutron channel is amplified through G_M^n , plus the magnetic production of the Δ^0 subsumed in the IC. A neutron with a very low initial momentum is excited to a Δ^0 which undergoes substantial final-state interactions in our kinematics. Now the $G_E^p G_M^p$ in the numerator of P'_x fails to compensate for such a large dilution in the cross-section, since both G_E^n and the transition G_E^* for Δ^0 are small.

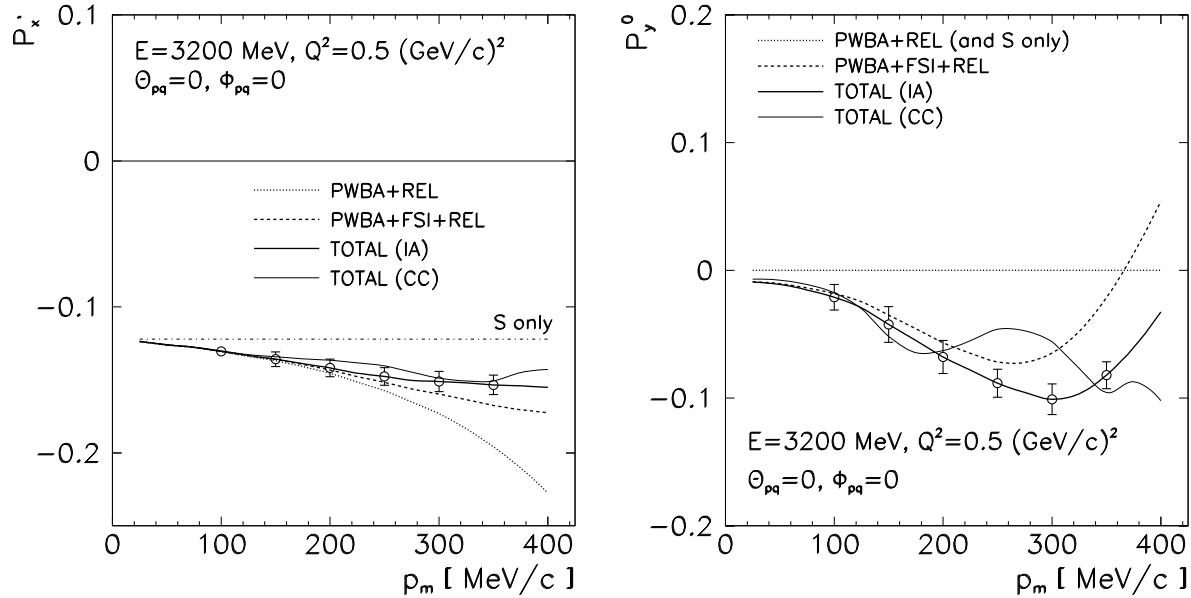


Fig. 8 — The p_m -dependence of P'_x and P_y^0 for parallel kinematics ($\theta = 0^\circ$) at $E = 3200$ MeV and $Q^2 = 0.5$ (GeV/c) 2 , with anticipated statistical uncertainties. The “S only” label corresponds to naive PWIA without the D -state.

The FSI also have a very characteristic p_m -dependence in P_y^0 which gives information on the imaginary part of the LT interference. This means that P'_x is sensitive to the treatment of spin-dependent FSI and the inclusion of isobars. Partly, the changes in P_y^0 as p_m increases reflect the distinct structures of the $L = 0$ and $L = 2$ (the “ D -state”) parts of FSI. A map of P_y^0 as a function of p_m yields a direct study of the spin-dependent final-state reaction mechanism.

Note that the polarization components themselves are ratios of the corresponding polarized and non-polarized parts of the cross-section (see Eqs. (1-2)), and as such are less prone to

cross-section systematics. An even cleaner picture emerges when instead of the individual recoil polarization components, their ratio is taken (see Fig. 9, left panel). For $p_m \lesssim 200$ MeV/c, the ratio has a very modest dependence: in a plane-wave picture, this region offers a method to extract G_E^p/G_M^p by using (3). The PWBA prediction is a relatively flat curve, implying that the D -state gives little effect on the nucleon form-factors, even at relatively high p_m . The small variation comes from neutron-channel contributions. If one ignores these, the naive PWIA (S -state only) and the PWBA are equivalent, in contrast to the individual components P'_x and P'_z where PWBA with inclusion of S - and D -state differs strongly from PWIA with S -state only. The FSI and the MEC+IC contributions also distort the ratio as p_m increases. In particular, the FSI signature is different in individual polarization components than it is in the ratio.

Figure 9 (right panel) shows the anticipated result of the double-polarization measurement at $p_m = 100$ MeV/c with the beam energies of 845 and 3200 MeV. Obviously, the polarization components P'_x and P'_z at 845 MeV are ~ 4 times larger than those at 3200 MeV. This means that the measurement of P'_x and P'_z at these two beam energies, with proton momentum and FPP parameters remaining constant, will serve as an excellent systematical cross-check.

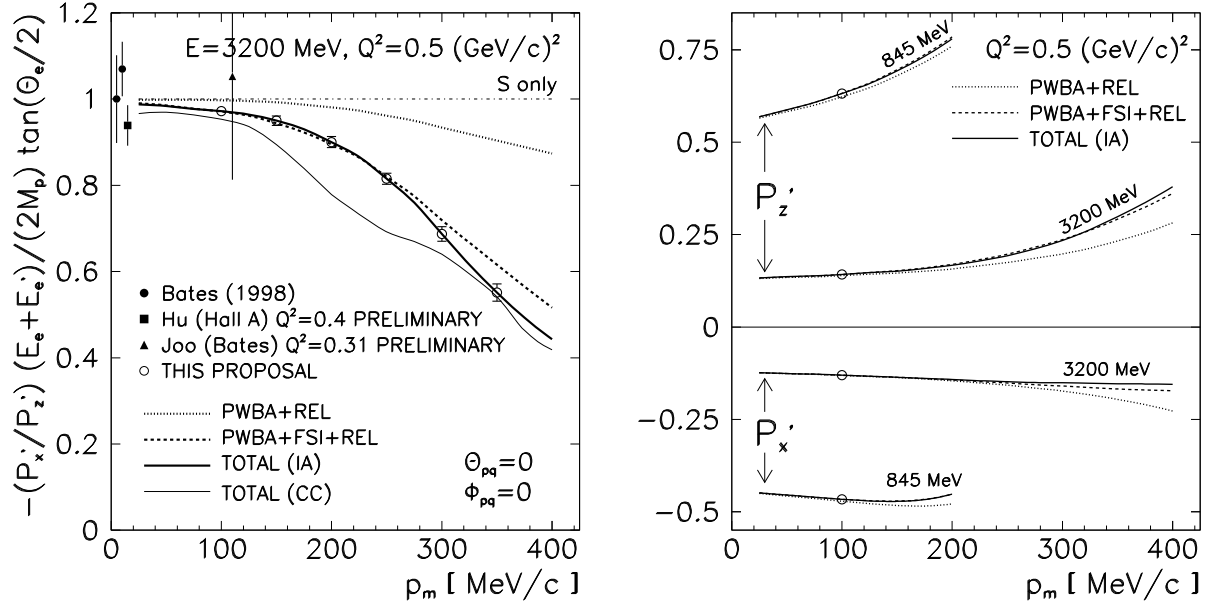


Fig. 9 — [LEFT] The p_m -dependence of the RHS of Eq. (3) at $\theta = 0^\circ$. The individual absolute uncertainties on P'_x and P'_z have been summed in the ratio. The “S only” label stands for naive PWIA without the D -state which is compared with PWBA+REL (S + D) and other models of Arehnhövel [24]. [RIGHT] The polarization components P'_x and P'_z as functions of p_m for beam energies of 845 and 3200 MeV, at $Q^2 = 0.5$ (GeV/c) 2 .

3.3 Parallel vs. perpendicular kinematics

We shall strictly maintain parallel kinematics as the reaction-mechanism effects are smallest at $\theta_{pq} = 0$. Parallel kinematics also gives the largest true count-rates and hence best statistics. In addition, the cross-sections [20, 22, 23] and recoil polarization components depend strongly on the reaction dynamics and consequently have strong angular dependencies due to oscillations of the Y_{2m} harmonics (see cross-section in Fig. 6, the panels of Fig. 10, as well as Refs. [12, 14, 18, 20]).

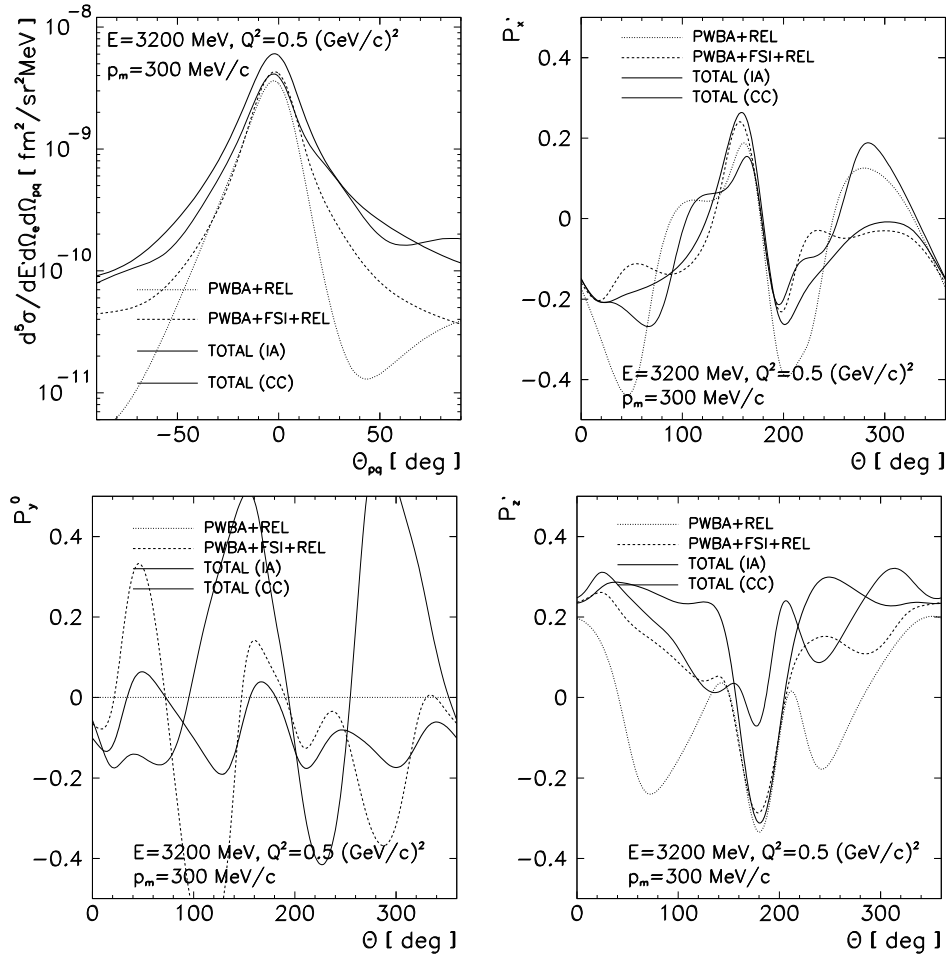


Fig. 10 — The angular dependence of the coincidence cross-section and proton polarization components for $E = 3200 \text{ MeV}$ and $Q^2 = 0.5 (\text{GeV}/c)^2$, at fixed $p_m = 300 \text{ MeV}/c$.

As shown by the formalism in Section 2, a combination of several structure functions contributes to the cross-section and the polarization components in perpendicular kinematics. A detailed study of the angular distributions would require a combination of left-right separation [18, 26, 27] and/or out-of plane detection [20, 28, 29]. At present, we limit our studies to parallel kinematics where the physics picture is simpler.

3.4 Separated structure functions

The Rosenbluth method by using two beam energies of 845 MeV and 3200 MeV will allow us to disentangle the longitudinal and transverse structure functions f_L and f_T for three values of missing momenta (100, 150, and 200 MeV/c). The lever-arm in the polarization of the virtual photon ε (ranging from ~ 0.3 to ~ 0.45 at 845 MeV to ~ 0.95 at 3200 MeV) is sufficient for a statistical uncertainty in the separated responses on the order of 1-2%. (For systematical uncertainties, see Table 5.) The separated responses are shown in Fig. 11. In order to divide out the sharp exponential momentum drop-off of the responses, the f_L and f_T are shown as ratios to $f_L(\text{PWBA+REL})$, which closely resembles $\rho(p)$, the momentum density distribution for the given NN-potential.

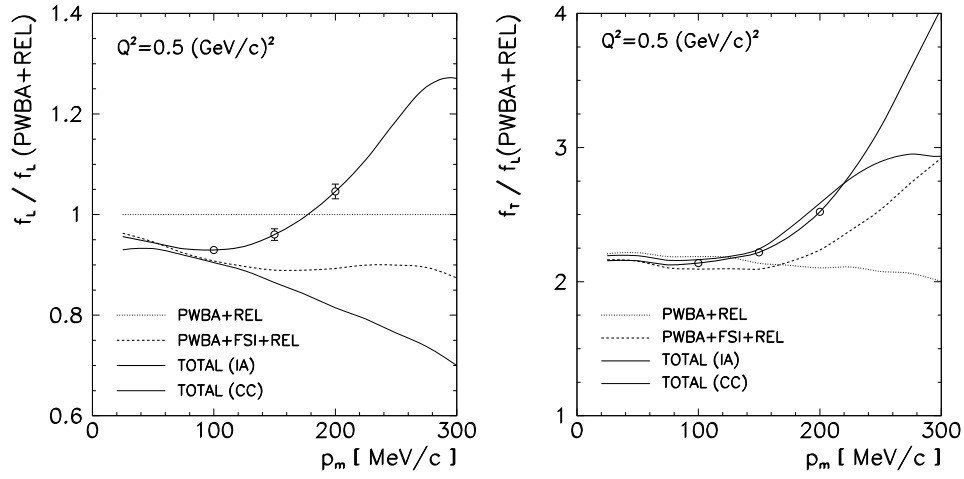


Fig. 11 — The separated f_L and f_T structure functions with expected statistical uncertainties. (For systematical uncertainties, see Table 5.) To divide out the sharp momentum drop-off of the responses, they are shown as ratios to $f_L(\text{PWBA}+\text{REL})$, which resembles the momentum density distribution.

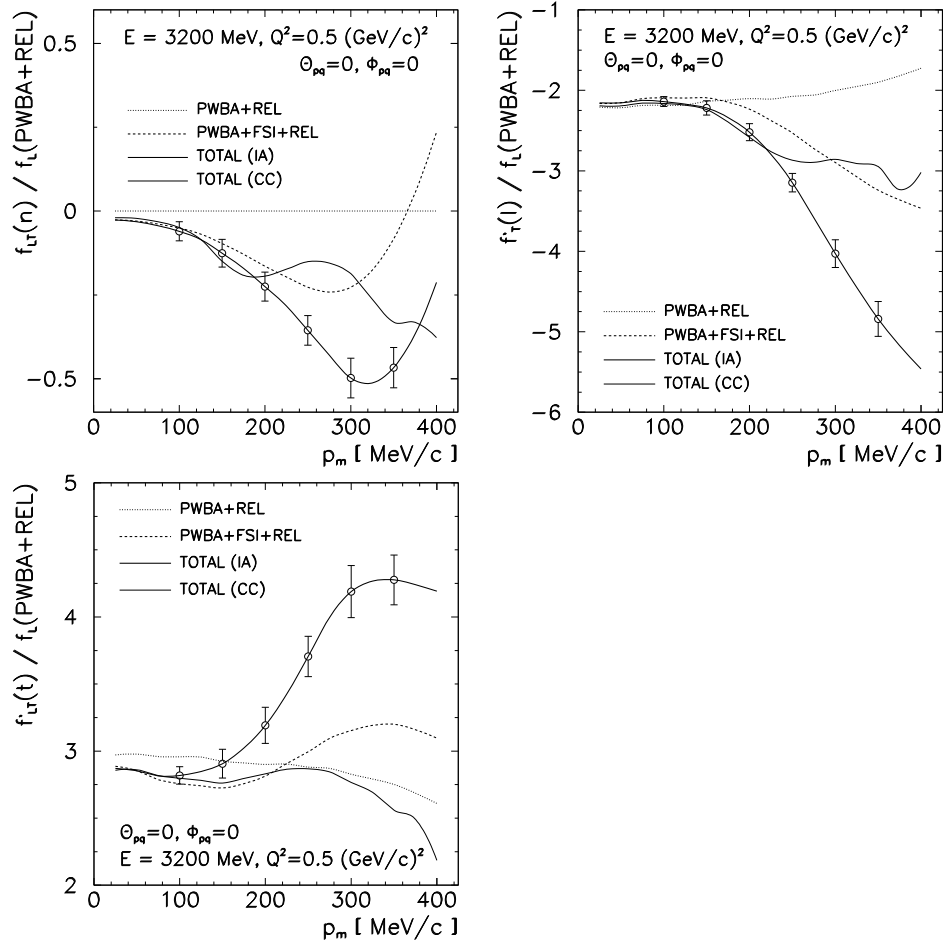


Fig. 12 — The responses f_{LT}^n (corresponding to P_y^0), f_T^l (corresponding to P_z'), and f_{LT}^t (corresponding to P_x') with expected relative statistical uncertainties. They are shown as ratios to $f_L(\text{PWBA}+\text{REL})$.

Fig. 12 shows the response functions f_{LT}^n , $f_T'^1$, and $f_{LT}'^t$, which correspond to the individual polarization components (see Eqs. (5-7)). They have also been divided by f_L (PWBA+REL).

As it has been discussed in Section 3, the reaction mechanism effects (and hence model-dependence) in f_L and f_T are small for $p_m \lesssim 100 \text{ MeV/c}$, while the region around $p_m = 200 \text{ MeV/c}$ lends itself for model studies. Additionally, while f_L and f_T yield the unpolarized momentum-density distribution, the polarization structure functions f_{LT}^n , $f_T'^1$, and $f_{LT}'^t$ provide the spin-dependent momentum distributions. They will constitute a strong test of the deuteron ground-state wave-functions and the reaction dynamics.

We wish to point out that extracting the structure functions in addition to just cross-sections and polarization components represents a considerable advantage since the physics ingredients enter the observables differently. For example, while there is almost no dependence on MEC+IC in P_z' , they have a tremendous influence on $f_T'^1$. This is due to the cancellation in the ratios when forming the polarization. Extracting the structure functions in addition to the polarization components therefore puts a more stringent test to modern theoretical models which need to account for all observables simultaneously.

The extracted polarization structure functions will also serve as a systematical cross-check of unpolarized f_L and f_T from the Rosenbluth separation. Namely, the systematic uncertainties are considered to be the main problem of traditional Rosenbluth experiments based on cross-section measurements.

4 Experimental equipment and methods

We plan to use a polarized beam with an energy of 3.2 GeV and the two High-Resolution Spectrometers (HRS) of Hall A. The electron scattering angles will be between 13° and 15° , while the ejected protons will be detected between 32° and 56° . (See Table 1 for kinematics.) The proton HRS is required to have FPP capability. The standard FPP configuration with variable thicknesses of graphite slabs ensures sufficient analysing powers for all proposed proton momenta. The standard cryogenic LD₂ target with a length of 15 cm will be used. With a beam current of $70 \mu\text{A}$, this corresponds to a luminosity of $3.33 \cdot 10^{38} / \text{cm}^2\text{s}$.

4.1 Focal-Plane Polarimeter

The ejected proton polarization will be detected in the focal plane polarimeter (FPP), located in the right arm HRS. This polarimeter has been used in many Jefferson Lab key experiments, and its operation presents no difficulty.

It consists of four blocks of graphite analyzer (“carbon doors”) of different thicknesses (1.5”, 3”, 6” and 9”) that can be opened or closed independently (in or out of the proton’s way) to allow for many different possible thicknesses ranging from 3.81 cm to 49.58 cm, to optimize the efficiency. The protons undergo a scattering in the analyzer, and asymmetries in the azimuthal angular distribution of this scattering are proportional to the two components of the polarization that are perpendicular to the momentum. The scattering angle is measured by detecting the incoming and outgoing tracks in two sets of straw chambers. The size and position of the rear chambers are optimized so that the geometrical efficiency for protons with

scattering angle up to 20° is almost 100%.

The azimuthal angular distribution of the scattering in the analyzer is given by

$$N^\pm(\vartheta, \varphi) = \frac{N_0}{2} \left[1 + (a_0 \pm A_y(\vartheta, T_p) P_x^{\text{fp}}) \cos \varphi + (b_0 \mp A_y(\vartheta, T_p) P_y^{\text{fp}}) \sin \varphi \right],$$

where $N^\pm(\vartheta, \varphi)$ is the number of protons hit by an incoming electron of helicity state (\pm) and scattering in the FPP at angles (ϑ, φ) , N_0 is the number of incoming protons in the FPP, $A_y(\vartheta, T_p)$ is the analyzing power of the graphite analyzer, and a_0 and b_0 are false asymmetries, induced by possible misalignment of the chambers and straw inefficiencies. The P_x^{fp} and P_y^{fp} are the two proton polarization components perpendicular to the momentum. Here, the \hat{z} -axis is defined along the particle momentum, the \hat{x} -axis is along the momentum dispersion direction, and $\hat{y} = \hat{z} \times \hat{x}$.

The helicity-dependent polarization transferred to the proton from the electron beam can be obtained by taking the difference between the two distributions for the $+$ and $-$ helicity states:

$$N^{\text{diff}} = \frac{N_0}{2} A_y(\vartheta, T_p) (P_x^{\text{fp}} \cos \varphi - P_y^{\text{fp}} \sin \varphi).$$

Note that the false asymmetries have disappeared, because we measure the transferred polarization. The helicity-independent, induced polarization is obtained by summing the two helicity state contributions:

$$N^{\text{sum}} = \frac{N_0}{2} \left[1 + (a_0 + A_y(\vartheta, T_p) P_x^{\text{fp}}) \cos \varphi + (b_0 - A_y(\vartheta, T_p) P_y^{\text{fp}}) \sin \varphi \right].$$

In this case, the false asymmetries must be determined by using unpolarized scattering off a hydrogen target, for which no asymmetry should arise (except for possible instrumental ones).

The analyzing-power angular distributions at a given kinetic energy are well known, from calibration data from Saclay, Jefferson Lab, and others. Note that we can also easily calibrate the analyzing powers for our momentum settings using elastic scattering of polarized electrons off a proton target.

The FPP measures the polarization of the proton at the focal plane of the spectrometer. To extract the three components P'_x , P'_z and P_y^0 , we need to transport this polarization back to the target and take into account the precession of the spin through the magnetic fields. In a perfect dipole approximation, the precession matrix is given by:

$$P_x^{\text{fp}} = -P'_z \sin \chi + P_y^0 \cos \chi \quad (8)$$

$$P_y^{\text{fp}} = P'_x \quad (9)$$

The precession angle χ is given by

$$\chi = (\mu_p - 1) \gamma \Theta_{\text{bend}},$$

where μ_p is the magnetic moment of the proton, γ is the relativistic boost and Θ_{bend} is the total bending angle inside the spectrometer.

In reality, we have to take into account event by event deviations from this perfect dipole approximation. The precession matrix becomes

$$\begin{pmatrix} P_x^{\text{fp}} \\ P_y^{\text{fp}} \\ P_z^{\text{fp}} \end{pmatrix} = \begin{pmatrix} S_{xx} & S_{xy} & S_{xz} \\ S_{yx} & S_{yy} & S_{yz} \\ S_{zx} & S_{zy} & S_{zz} \end{pmatrix} \begin{pmatrix} P'_x \\ P_y^0 \\ P'_z \end{pmatrix}.$$

The coefficients S_{ij} are calculated using the external code COSY, and the polarization components at the target are extracted using a maximum-likelihood method. This analysis method has been extensively used for this polarimeter. In polarization measurements, the main source of systematic error lies in the uncertainty in the precession of the polarization. Careful alignment studies of the HRS magnetic elements have been performed [30], and the precession code COSY has been optimized so that eventually, the total uncertainty of the measurement is mostly dominated by the statistics (see below for details).

The statistical uncertainties on the asymmetries measured in the FPP, thus on the polarization components, are given by

$$\Delta P_x^{\text{fp}} = \Delta P_y^{\text{fp}} = \sqrt{\frac{2}{N_0 f}}.$$

Here f is the figure of merit of the polarimeter, given by

$$f = \int_{\vartheta_{\min}}^{\vartheta_{\max}} \epsilon(\vartheta) A_y^2(\vartheta) d\vartheta,$$

where $\epsilon(\vartheta)$ is the efficiency of the polarimeter at a given scattering angle. Translated to target quantities, the error becomes, according to Eqs. (8-9):

$$\Delta P'_x = \frac{1}{P_e} \sqrt{\frac{2}{N_0 f}}, \quad (10)$$

$$\Delta P_y^0 = \frac{1}{\cos \chi} \sqrt{\frac{2}{N_0 f}}, \quad (11)$$

$$\Delta P'_z = \frac{1}{P_e} \frac{1}{\sin \chi} \sqrt{\frac{2}{N_0 f}}. \quad (12)$$

Table 2 lists the proton kinetic energy, the analyzer thickness, the energy lost in the graphite, the precession angle, the FPP efficiency, analyzing power and figure of merit at each kinematics. The efficiency and analyzing power are extrapolation from Saclay data [31], and have been confirmed by the Hall A FPP in the past.

Table 2 — Simulated FPP parameters for different proton kinetic energies corresponding to the proposed values of p_m : optimal thickness of carbon “door” ^{12}C , energy loss E_{loss} , precession angle χ , overall efficiency ϵ , analyzing power A_y , and the figure of merit f . The simulation is based on the extrapolation of the data from Saclay [31].

p_m [MeV/c]	T_p [MeV]	^{12}C [cm]	E_{loss} [MeV]	χ	ϵ	A_y	f
100	360	19.05 (7.5")	93	111°	10.0%	0.41	$17.6 \cdot 10^{-3}$
150	417	22.86 (9")	102	116°	11.9%	0.37	$16.8 \cdot 10^{-3}$
200	486	22.86 (9")	95	122°	13.6%	0.32	$14.4 \cdot 10^{-3}$
250	569	30.48 (12")	114	129°	15.9%	0.28	$12.1 \cdot 10^{-3}$
300	675	34.29 (13.5")	122	138°	17.6%	0.27	$11.2 \cdot 10^{-3}$
350	812	49.58 (19.5")	166	150°	17.5%	0.23	$10.5 \cdot 10^{-3}$

Overall, in our kinematic region we have excellent figures of merit and favourable spin-precession angle to the FPP to allow good measurements of all three polarization components.

4.2 FPP systematical uncertainties

As focal-plane polarimetry involves ratios of polarized and unpolarized parts of the cross-section, many systematical errors are suppressed. The remaining uncertainties linked to the polarimeter are small compared to the statistical uncertainties. First, some error may arise from uncertainties in the scattering angle in the FPP. A 1 mrad precision in the determination of this angle leads to uncertainties of the order of 1% in the polarization. The second source of systematic uncertainties is the treatment of the precession inside the spectrometer. Careful studies of the alignment of the magnetic elements have reduced the associated error to the percent level [30]. Also, for the transferred part of the polarization, the uncertainty of the beam polarization must be taken into account. The beam polarization will be measured continuously with the Hall A Compton polarimeter, with the combined statistical and systematical errors on the order of 1.3% (values determined in E91-011 [32]). So the overall systematic error on the polarization measurement is anticipated to be below 3%, which is better than the statistical accuracy. The *relative* statistical uncertainties on the individual polarization components will be on the order of 5% for P'_x and P'_z , and 10% or more for P_y^0 (see Section 5 below), which is still larger than the systematical uncertainty arising from the polarization measurement itself. Hence the proposed measurement of polarization components is still limited by the statistical uncertainty, and we estimate our beam-time request to be modest.

5 Counting rates and beam-time request

The single count rates were estimated with the computer codes EPC and QFSV of Lightbody and O'Connell [33] as built into the simulation package MCEEP and are listed in Table 3. The accidental rates have been computed in MCEEP by assuming a coincidence time window of 40 ns. In the estimate for the accidentals rate with software cuts we have assumed a factor of 1/10 due to the true coincidence-time peak width of 4 ns vs. the 40 ns time-window; a factor of 1/10 due to the missing-mass interval of ~ 10 MeV compared to the ~ 100 MeV phase-space over which the accidentals are distributed relatively smoothly; and a factor of 1/10 originating in vertex cuts. (For the electron HRS positioned at $\sim 14^\circ$, the vertex-z resolution deteriorates from the intrinsic ~ 1.5 mm to ~ 6 mm, with singles uniformly distributed along the target cell. If the corresponding proton vertex from the hadron HRS does not coincide with the ~ 6 mm electron vertex range, it can be excluded.) Since these three assumptions are quite conservative, we expect the physics accidentals to be suppressed by a factor of $\sim (1/10)^3 = 1/1000$ with respect to the trues. We therefore have excellent physics trues-to-accidentals ratios in the entire kinematic region.

Table 4 gives the coincidence count-rate estimates and the beam-time request. The count rates have been calculated using MCEEP, with an 80% polarized, $70 \mu\text{A}$ electron beam and a 15 cm long cryogenic deuterium target. The maximum beam current is limited by the raw accidental rates (less than 2 kHz) in the data-acquisition system. Delivery of such polarization and high current is expected at JLab within months, with installation of the new gun at the injector. The σ_1^{cc} prescription for the off-shell e-p cross-section and a parameterization of the nucleon momentum density distribution calculated by van Orden are incorporated into MCEEP. The simulation output was scaled to Arenhövel's calculations of $d(e, e'p)$ scattering to take into account the reaction mechanisms. The scaling factor varies from 1.4 to 2.3. The count rates are consistent with the ones obtained in experiment E89-028, at $p_m = 0$ and $Q^2 = 0.4 (\text{GeV}/c)^2$.

Table 3 — Estimates of singles, accidental (without and with software cuts), and true coincident rates for the proposed kinematics with beam energies of 845 MeV (first three rows) and 3200 MeV (remaining rows), with a beam current of $I_e = 70 \mu\text{A}$. The Left HRS is for electrons, the Right HRS is for protons.

p_m [MeV/c]	θ_e [°]	θ_p [°]	Singles				Accid.	Accid. [†]	Trues
			(e) [kHz]	(π^-) [kHz]	(p) [kHz]	(π^+) [kHz]	(raw (ep)) [Hz]	(ep) [Hz]	(ep) [Hz]
100	67.7	33.6	< 1	5	4	7	0.1	$\ll 1$	87
150	73.6	28.5	< 1	5	3	8	0.04	$\ll 1$	10
200	83.2	22.5	< 1	5	5	13	0.05	$\ll 1$	1.4
100	13.5	56.1	462	54	33	33	1237	1	1250
150	13.6	52.1	195	57	40	34	628	1	459
200	13.8	47.6	135	59	47	35	510	1	133
250	14.1	42.8	188	60	57	36	867	1	50
300	14.4	37.6	316	61	67	38	1728	2	25
350	14.9	32.1	288	61	78	39	1830	2	12

[†] with cuts (see text for details)

Table 4 — The coincidence rates, absolute statistical uncertainties on the recoil polarization components, and the beam-time request for production runs at $I_e = 70 \mu\text{A}$. Parallel kinematics has been enforced in the simulation by using a $\theta_{pq}^{\text{CM}} < 10^\circ$ cut.

E_e [MeV]	p_m [MeV/c]	(e, e'p) [Hz]	$\Delta P'_z$	ΔP_y^0	$\Delta P'_x$	Beam time [h]
845	100	87	0.009	0.016	0.007	10
845	150	10	n/a	n/a	n/a	2
845	200	1.4	n/a	n/a	n/a	8
3200	100	1250	0.004	0.010	0.003	2
3200	150	459	0.006	0.014	0.005	4
3200	200	133	0.007	0.013	0.006	10
3200	250	50	0.007	0.011	0.006	32
3200	300	25	0.010	0.012	0.007	46
3200	350	12	0.013	0.011	0.007	100
FPP calibration						17
Møller						8
Beam energy						4
Total						243

The electronic and computer deadtimes could be a minor problem at kinematics with $p_m = 300$ and 350 MeV/c , but it can be resolved on-line by slightly narrowing the coincidence-time window.

5.1 Systematical uncertainties

We wish to emphasize that the uncertainties on the individual polarization components listed in Table 4 are absolute. The corresponding relative uncertainties are on the order of 5% for P'_x and P'_z , and 10% or worse for P_y^0 (see below). Except for the Rosenbluth part, the proposed experiment is therefore still limited by the statistical uncertainty. This means that for the physics goal we wish to achieve, we are not over-requesting beam hours.

The uncertainty on the P'_x is smaller relatively to P'_z because the former does not contain the precession factor (see Eqs. (10-12)). Larger beam times for increasing values of p_m are partly due to the precession angle approaching 180° (see Table 2). The use of COSY and the maximum-likelihood analysis method significantly reduce the effect of the precession, but this correction is being studied.

Table 5 shows the expected overall statistical and systematical uncertainties on the individual structure functions accessible to this experiment. The Rosenbluth separation of f_L and f_T is not statistically limited: with the yields sufficient for a precise determination of the polarization components (see Table 4), the cross-sections at individual E_e and p_m are known statistically to mere fractions of a %. Assuming an additional 2% systematical uncertainty on the cross-section level then translates into systematical uncertainties of 4-6% on f_T and 9-11% on f_L .

Table 5 — Anticipated relative statistical and systematical uncertainties on f_L and f_T , and the statistical uncertainties on the polarization structure functions $f_T^{\prime 1}$, f_{LT}^n , and $f_{LT}^{\prime t}$. The systematical uncertainties of the latter three are discussed in Subsection 4.2. We assume a 2% systematical uncertainty on the cross-sections.

p_m [MeV/c]	$\Delta f_L/f_L$ [%]	$\Delta f_T/f_T$ [%]	$\Delta f_T^{\prime 1}/f_T^{\prime 1}$ [%]	$\Delta f_{LT}^n/f_{LT}^n$ [%]	$\Delta f_{LT}^{\prime t}/f_{LT}^{\prime t}$ [%]
100	± 0.2 (± 10.6)	± 0.2 (± 6.5)	± 3	± 47	± 2
150	± 1.2 (± 10.6)	± 0.8 (± 5.0)	± 4	± 33	± 4
200	± 1.4 (± 8.8)	± 0.9 (± 3.9)	± 4	± 19	± 4
250	n/a	n/a	± 4	± 12	± 4
300	n/a	n/a	± 4	± 12	± 5
350	n/a	n/a	± 4	± 13	± 4

By measuring the polarization structure functions besides the f_L and f_T , we shall have an additional cross-check on the systematic uncertainties possibly associated with the traditional Rosenbluth cross-section measurements. For the polarization structure functions $f_T^{\prime 1}$, f_{LT}^n , and $f_{LT}^{\prime t}$, only the statistical errors are listed in the Table. Their systematical uncertainties have been discussed at length in Subsection 4.2. They are typically between 2 and 3% depending on the individual components.

6 Conclusions

We propose a high-precision measurement of proton recoil polarization components in the $d(\bar{e}, e'\bar{p})$ at $Q^2 = 0.5 \text{ (GeV/c)}^2$ in parallel kinematics, in a broad range of missing momenta. The individual components P'_x and P'_z will be used to probe the spin structure of the deuteron, while the P_y^0 and the P'_x/P'_z provide spin-dependent reaction dynamics studies. Modern models surprisingly suggest that the D -state has little effect when the P'_x/P'_z ratio is used to extract information on the electric form-factors, even at high missing momenta. On the other hand, the predicted effects from the spin-dependent reaction mechanism are enormous.

Measurements of the individual polarization components P'_x and P'_z lead directly to the f'_{LT} and $f_T^{\prime 1}$ spin-dependent structure functions of the deuteron. They show a close link between the proton form-factors (at low p_m) and the deuteron spin structure (at high p_m), and demonstrate to what extent the deuteron can be used as an effective neutron target.

By combining both the Rosenbluth separation and the polarization measurements, one can provide a precise and complete picture of the deuteron in terms of both spin-independent and spin-dependent momentum-density distributions. A detailed study of these is extremely important to learn when the deuteron can be used as an effective neutron target, and also for the few-body physics.

References

- [1] T. W. Donnelly, A. S. Raskin, *Ann. Phys.* **169** (1986) 247.
- [2] A. Picklesimer, J. W. van Orden, *Phys. Rev. C* **35** (1987) 226.
- [3] H. Arenhövel, W. Leidemann, E. L. Tomusiak, *Phys. Rev. C* **52** (1995) 1232;
Phys. Rev. C **46** (1992) 455.
- [4] J. L. Forest et al., *Phys. Rev. C* **54** (1996) 646.
- [5] J. A. Tjon, *Few-Body Systems Suppl.* **5** (1992) 17;
E. Hummel, J. A. Tjon, *Phys. Rev. C* **42** (1990) 423; **49** (1994) 21.
- [6] B. Mosconi, P. Ricci, *Nucl. Phys. A* **517** (1990) 483;
B. Mosconi, J. Pauschenwein, P. Ricci, *Phys. Rev. C* **48** (1993) 332.
- [7] G. Beck, H. Arenhövel, *Few-Body Systems* **13** (1992) 165 (1992);
Th. Wilbois, G. Beck, H. Arenhövel, *Few-Body Systems* **15** (1993) 39;
F. Ritz, H. Göller, Th. Wilbois, H. Arenhövel, *Phys. Rev. C* **55** (1997) 2214.
- [8] S. Jeschonnek, T. W. Donnelly, *Phys. Rev. C* **59** (1999) 2676;
S. Jeschonnek, *Phys. Rev. C* **63** (2001) 034609.
- [9] I. Passchier et al., *Phys. Rev. Lett.* **88** (2002) 102302.
- [10] H. Arenhövel, W. Leidemann, E. L. Tomusiak, *Z. Phys. A* **331** (1988) 123;
errata *ibid.* **334** (1989) 363.

- [11] B. D. Milbrath et al. (Bates FPP Collaboration), Phys. Rev. Lett. **80** (1998) 452;
errata ibid. **82** (1999) 2221;
comment ibid. **81** (1998) 2831.
- [12] D. Barkhuff et al., Phys. Lett. B **470** (1999) 39.
- [13] K. Joo, PhD Thesis, Massachusetts Institute of Technology (1997);
submitted for publication.
- [14] B. Hu et al., submitted to Phys. Rev. Lett.
- [15] M. van der Schaar et al., Phys. Rev. Lett. **66** (1991) 2855.
- [16] J. E. Ducret et al., Phys. Rev. C **49** (1994) 1783.
- [17] D. Jordan et al., Phys. Rev. Lett. **76** (1996) 1579.
- [18] S. Gilad, W. Bertozzi, Z.-L. Zhou, Nucl. Phys. A **631** (1998) 276c.
- [19] R. Böhm et al., submitted to Eur. Phys. J. A.
- [20] A. Pellegrino et al., Phys. Rev. Lett. **78** (1997) 4011.
- [21] W.-J. Kasdorp et al., Phys. Lett. B **393** (1997) 42;
W.-J. Kasdorp et al., Few-Body Systems **25** (1998) 115.
- [22] K. I. Blomqvist et al., Phys. Lett. B **424** (1998) 33.
- [23] P. E. Ulmer et al., Phys. Rev. Lett. **89** (2002) 062301.
- [24] H. Arenhövel, private communication.
- [25] R. Machleidt, Phys. Rev. C **63** (2001) 024001.
- [26] H. J. Bulten et al., Phys. Rev. Lett. **74** (1995) 4775.
- [27] W. Bertozzi, Z.-L. Zhou (spokespersons), JLab Proposal PR-97-107.
- [28] Z.-L. Zhou et al., Phys. Rev. Lett. **87** (2001) 172301.
- [29] K. Wang, B. E. Norum, W. Bertozzi, T. Tamae (spokespersons), JLab Proposal E-02-101.
- [30] L. Pentchev, J. J. LeRose, *Quadrupole alignment studies in the HRSs*, JLab-TN-01-052
(2001).
- [31] B. Bonin et al., Nucl. Instr. Meth. A **288** (1990) 379.
- [32] S. Escoffier, PhD Thesis, Paris XI, France (2001);
JLab-TN-01-052 (2001).
- [33] J. Lightbody, J. S. O'Connell, Computers in Physics **2** (1988) 57.